ORIGINAL RESEARCH ARTICLE

Synthesis and Characterization of an Fe/Co Ferrite Spinel Oxide Film Produced by Using N_2/Steam Heat Treatment on Two Maraging Steels

MAURO ANDRES CERRA FLOREZ, GEMMA FARGAS RIBAS, JOAN JOSEP ROA ROVIRA, ANTONIO MANUEL MATEO GARCÍA, STEPHANY APARECIDA SANTOS DA MATA, ENRIQUE RODRÍGUEZ-CASTELLÓN, and MARCELO JOSÉ GOMES DA SILVA

An experimental procedure was developed to obtain an oxide layer formed mainly by spinel on maraging steels. It consists of different stages with specific conditions, such as atmospheres rich in nitrogen and water vapor, and different steps of temperatures and times. Tests were performed on grade 300 and 350 maraging steels. Oxide layer characterization was done using optical and electron microscopy, spectroscopy, X-ray diffraction, and nanoscratch tests in order to determine the adhesion force as well as to observe the main deformation mechanism induced under sliding tests. In both steels, oxide layers are formed by the spinel's Fe_3O_4 and $CoFe_2O_4$ in amounts close to ca. 85 pct, whereas TiO_2 and MoO_3 represent the other 15 pct. No hematite was found. The low oxygen availability during the heat treatment was fundamental for avoiding hematite formation. A nickel-rich austenitic phase formed at the metal-oxide interface due the kinetics of the oxidation process of the cobalt, iron, and molybdenum. The particular conditions of the heat treatments induced the formation of a mixture of iron, nickel, and cobalt spinel ferrites, thereby contradicting previous studies that said that only magnetite would be formed. The sliding tests at the nanometric length scale highlight that the layer formed on maraging 300 grade presents a better adhesion than the other investigated material due to the fact that it requires more load in order to induce cracks located at the edge of the sliding track and, subsequently, the chipping of the formed layer.

MAURO ANDRES CERRA FLOREZ is with the LACAM - Departament of Metallurgical and Materials Engineering, Universidade Federal do Ceará, Campus do Picí, bloco 729, Fortaleza, 60440-554, Brazil and also with the CIEFMA - Department of Materials Science and Engineering, Barcelona Research Center in Multiscale Science and Engineering, Universitat Politécnica de Catalunya, Escola d'Enginyeria de Barcelona Est (EEBE), Eduard Maristany 10-14, 08019 Barcelona, Spain. Contact e-mail: mauro.cerra@gmail.com GEMMA FARGAS RIBAS, JOAN JOSEP ROA ROVIRA, ANTONIO MANUEL MATEO GARCÍ A are with the CIEFMA - Department of Materials Science and Engineering, Barcelona Research Center in Multiscale Science and Engineering, Universitat Polité cnica de Catalunya, Escola d'Enginyeria de Barcelona Est (EEBE) STEPHANY APARECIDA SANTOS DA MATA and MARCELO JOSÉ GOMES DA SILVA are with the LACAM - Departament of Metallurgical and Materials Engineering, Universidade Federal do Ceará. ENRIQUE RODRÍGUEZ-CASTELLÓN is with the Department of Inorganic Chemistry, Crystallography and Mineralogy, University of Malaga, Campus de Teatinos, 29071 Málaga, Spain.

Manuscript submitted August 25, 2021; accepted December 23, 2021. Article published online February 9, 2022

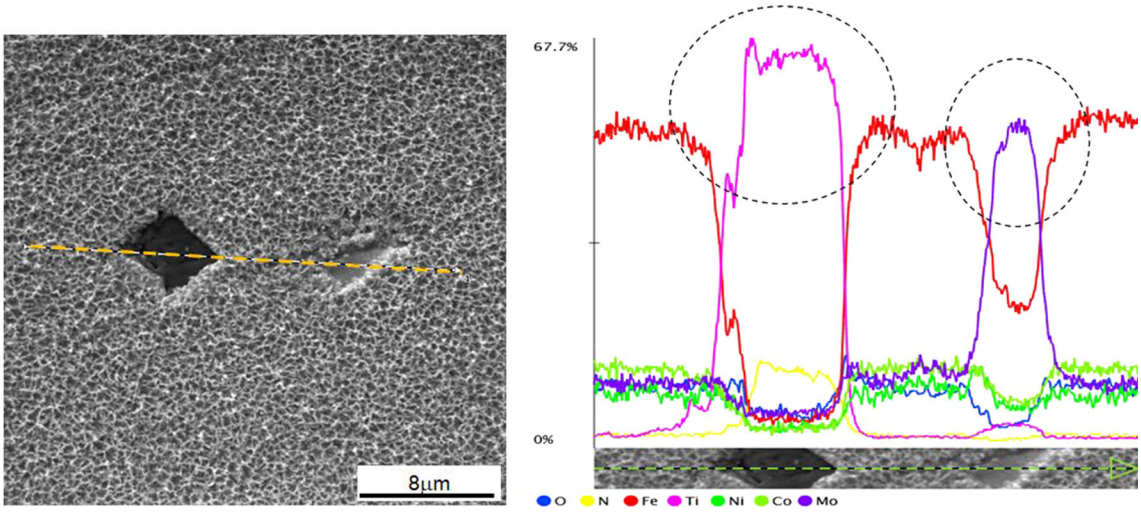

https://doi.org/10.1007/s11661-022-06588-3

I. INTRODUCTION

THE chemical composition of maraging steels, with 18 pct Ni, 7 to 12 pct Co, 3 to 5 pct Mo, 0.2 to 1.6 pct Ti, and ultralow carbon content, allows for hardening by precipitation of nanometric intermetallic phases during aging treatments. Thus, maraging steels have particular properties arising from the combination of a martensitic matrix and those fine intermetallic precipitates, such as Ni_3(Ti,Mo) and Fe_2(Ti,Mo).[1–9] These properties make them very attractive materials for aeronautic, aerospace, and military applications, and also for applications where components are in contact with highly corrosive fluorinated compounds, such as in uranium enrichment ultracentrifuges.[1,9–13] Barzashka and Oelrich[12] appear to be the only authors that have reported a preoxidation process of the components of the ultracentrifuges manufactured with maraging steel, where atmospheres with steam are used to form an oxide layer that prevents corrosion resistance. But there are no specifications about this process or about the characteristics of the oxide formed.

Four other works were developed prior to the 1990s studying the oxidation processes of maraging steels in different atmospheres to produce spinel-type oxides. Three of these works were developed by Klein *et al.*[14–16] The first one studied the thermodynamics and kinetics of the chemical reactions for the production of oxides in a maraging steel, and also in a Kovar steel, using an atmosphere with superheated steam at temperatures close to 773.15 K (500 °C). As a result, they observed the formation of Fe_3O_4 iron spinel (magnetite) and the possibility of nickel and cobalt within the oxide film. In the second work, the same steels were subjected to an aging treatment at 758.15 K (485 °C) for 3 hours, under three different atmospheres of water vapor, CO_2, and O_2, respectively. For all atmospheres, the results showed the formation of a layer between 2 and 3 μm, composed solely of magnetite, and a metal-oxide interface rich in nickel and cobalt. In the third study published by Klein *et al.*,[15] samples of maraging 250, pure titanium, and pure molybdenum were subjected to 758.15 K (485 °C) for 3 hours to relate the oxidation processes of these elements with the compounds found in the oxide of maraging steel. It was found that titanium and molybdenum oxidize in the initial stages and, due to thermodynamic and kinetic conditions, remain in the inner parts of the film, covered by magnetite.

The fourth work was developed by Rezek *et al.*,[17] who studied the oxidation of maraging steel 250 during the aging treatment at 758.15 K (485 °C) for 3 hours using an atmosphere with superheated steam. The steam flow was changed to analyze its influence on the composition of the oxide. Thus, it was found that the largest flux gives rise to a greater amount of magnetite. However, for all conditions, an unwanted Fe_2O_3 phase (hematite) was formed.

No additional publications about this topic were found, and in this context, the present investigation intends to produce an oxide with the largest amount of spinel. Moreover, the conditions of temperature, time, and atmosphere were selected to avoid the formation of hematite. An experimental procedure has been established (based on the work of Florez *et al.*[18]) that can be

Table I. Chemical Composition (Weight Percent) of Grade 300 and Grade 350 Maraging Steels

Steel	Fe	Ni	Co	Mo	Ti	Cr	V	Si	Al	C
Mar300	bal	18.28	9.51	4.80	0.73	0.12	0.10	0.08	0.07	< 0.01
Mar350	bal	17.65	11.65	4.69	1.44	0.05	0.10	0.04	0.06	0.002

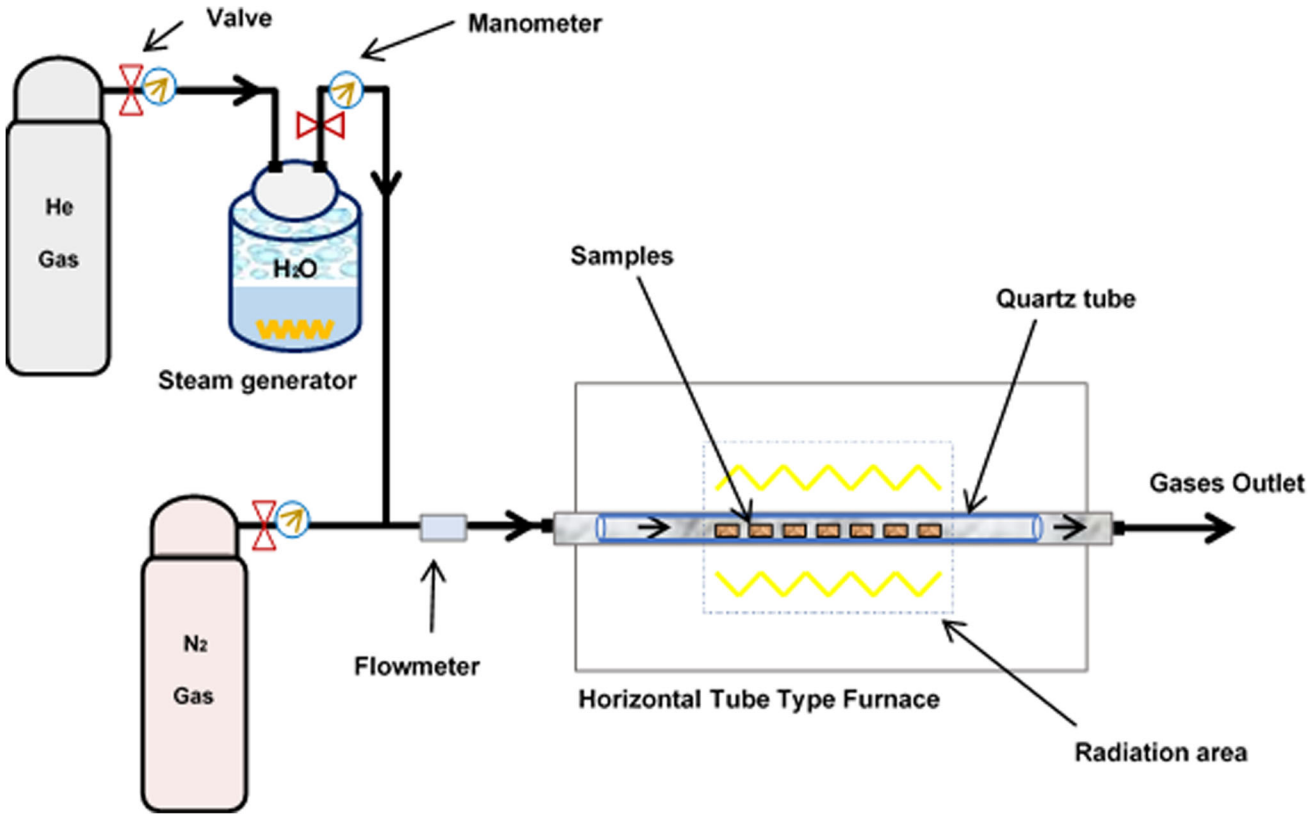

Fig. 1—Experimental configuration of the devices for the aging heat treatment.

reproduced under basic laboratory conditions. The main objective of this work is focused on verifying if the conditions of the heat treatment and the chemical composition of the steels used are sufficient for the formation and growth of a spinel-type oxide on the surface of the steels. A horizontal tubular oven, nitrogen gases, and steam were used in the different stages of the thermal aging treatment of maraging steel grades 300 and 350.

II. MATERIALS AND METHODS

Samples of maraging steel, grades 300 and 350 (whose chemical compositions are summarized in Table I), were used for the present study. Their dimensions were $2 \times 1 \times 1\ cm^3$. These samples were solution annealed at 1113.15 K (840 °C) for 1 hour in a muffle furnace, air cooled, and then polished with SiC paper. A Philips X'Pert X-ray diffractometer (Philips, Almelo, The Netherlands) with Co K_α radiation and a monochromator was used for determining the phases present after the solution annealing treatment. The angular parameter 2θ ranged between 30 and 110 deg, with an angular step of 0.02 deg per scan and a counting time of 3 seconds. The voltage and current used were 40 kV and 45 mA, respectively. The analysis of the XRD results was performed using the X'PERT HIGHSCORE PLUS* program provided by Panalytical.

*X'PERT HIGHSCORE PLUS is a trademark of Panalytical (Almelo, The Netherlands).

The aging treatments were carried out in a horizontal tube oven with gas inlet and outlet. For the oxidation process, the inlet to the furnace had two connections, one connected to a steam generator and the other to N_2 cylinders. The steam generator reached a temperature of 423.15 K (150 °C) and it was necessary to use helium injection as a carrier gas to increase the flow rate up to 600 mL/min. The flow of all gases was measured with a

flowmeter. This experimental setup can be seen in Figure 1.

The samples of each steel grade (in two different experiments) were placed in a quartz tube, introduced inside the oven and then heated at 573.15 K (300 ºC) for 30 minutes under N_2 atmosphere (400 mL/min). Steam was added and the temperature increased for 15 minutes up to 763.15 K (490 ºC). Shortly thereafter, N_2 gas was removed and the temperature was kept constant at 763.15 K (490 ºC) for 3 hours with only the steam/helium atmosphere (600 mL/min). After this aging treatment, the samples were cooled with a constant N_2 flow (400 mL/min) for 3 hours to avoid their overoxidation.

After the heat treatments, the surface of the samples was characterized using different advanced techniques to understand the oxidation process and elucidate the different phases formed. A Carl ZEISS LSM 800 (Carl Zeiss, Oberkochen, Germany) laser scanning confocal microscope and an atomic force microscope (Dimension D3100) (Veeco Instruments, Plainview, NY, USA) were used to observe the surface morphology. Oxide roughness was observed by atomic force microscopy (AFM), and the resulting images and roughness analyses were conducted using WSxM 5.0 software, developed by Horcas et al.[19] To completely assess the surface topography, several parameters were evaluated: average roughness (R_a), maximum vertical height between the highest peak and the lowest valley (R_z), maximum peak height (R_p), and maximum valley depth (R_v). More information about the mathematical and physical definitions of these roughness parameters, as well as their respective equations, is summarized in References 20–22.

For the identification of the components presents on the oxide layer, X-ray diffraction (XRD) measurements, Raman spectroscopy, and X-ray photoelectron spectroscopy (XPS) were used. The XRD was used in the low-angle/grazing incident configuration and the following parameters: 3 deg as grazing incidence angle, angular parameter 2θ ranging between 10 and 80 deg, angular step of 0.02 deg per scan and counting time of 3 seconds, and voltage and current of 40 kV and 45 mA, respectively. The results were analyzed using the X'PERT HIGHSCORE PLUS software and the quantification of the phases was done using the reference intensity ratio (RIR) based in the Chung methodology[23] and mentioned by Zhou *et al.*[24] The Raman spectroscopy was performed on the Renishaw's inVia Qontor Raman microscope (Renishaw, Gloucestershire, UK) with a neon laser with $\lambda \sim 532$ nm, with intensity analysis performed in the RAMAN ENVIRONMENT (WIRE)** software.

**RAMAN ENVIRONMENT (WIRE) is a trademark of Renishaw (Gloucestershire, UK)

Finally, the XPS measurements were performed on the Physical Electronics spectrometer (PHI Versa Probe II Scanning XPS Microprobe) (Physical Electronics, Inc, Chanhassen, MN, USA) with monochromatic X-ray radiation Al K_α (1400 μm, 26.6 W, 5 kV, and 1486.6 eV) and a double beam neutralizer. The experiments were carried out after cleaning the surface for two pickling cycles with argon (Ar^+) ions at 0.5 eV for 1 minute and 1 keV for 5 minutes, respectively. XPS spectra were processed using the MultiPak 9.0 package (Physical Electronics, Inc, Chanhassen, MN, USA). The binding energy values were referenced to the C 1*s* adventitious signal at 284.8 eV and the recorded spectra were fitted using Gauss–Lorentz curves. The atomic concentration percentages of the constituent elements

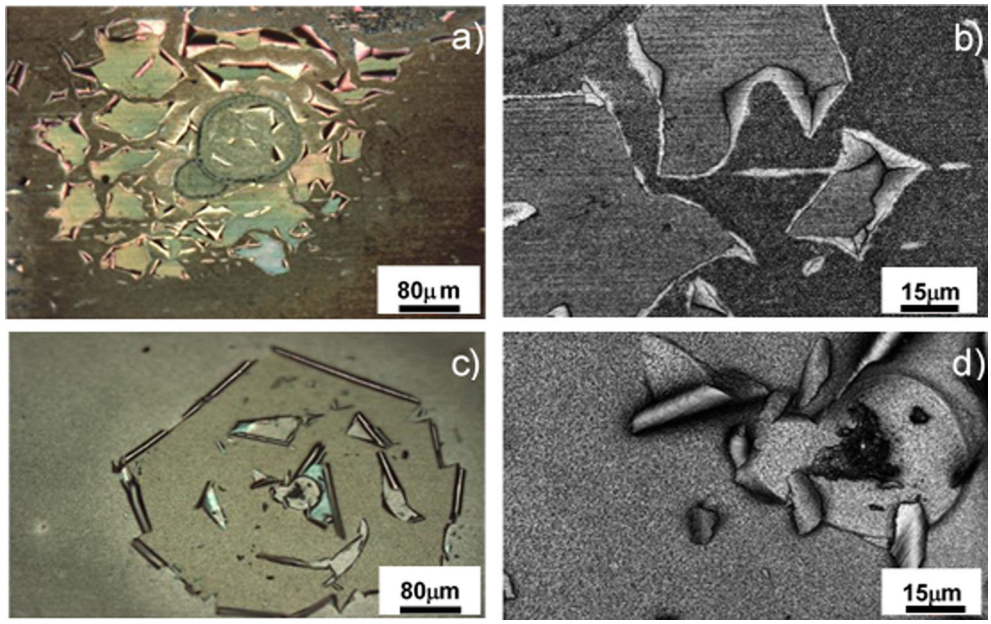

Fig. 2—(*a*) and (*c*) Optical and (*b*) and (*d*) LSCM micrographs of the heterogeneities found on the oxide layer for (a) and (b) grade 300 and (c) and (d) grade 350 maraging steels.

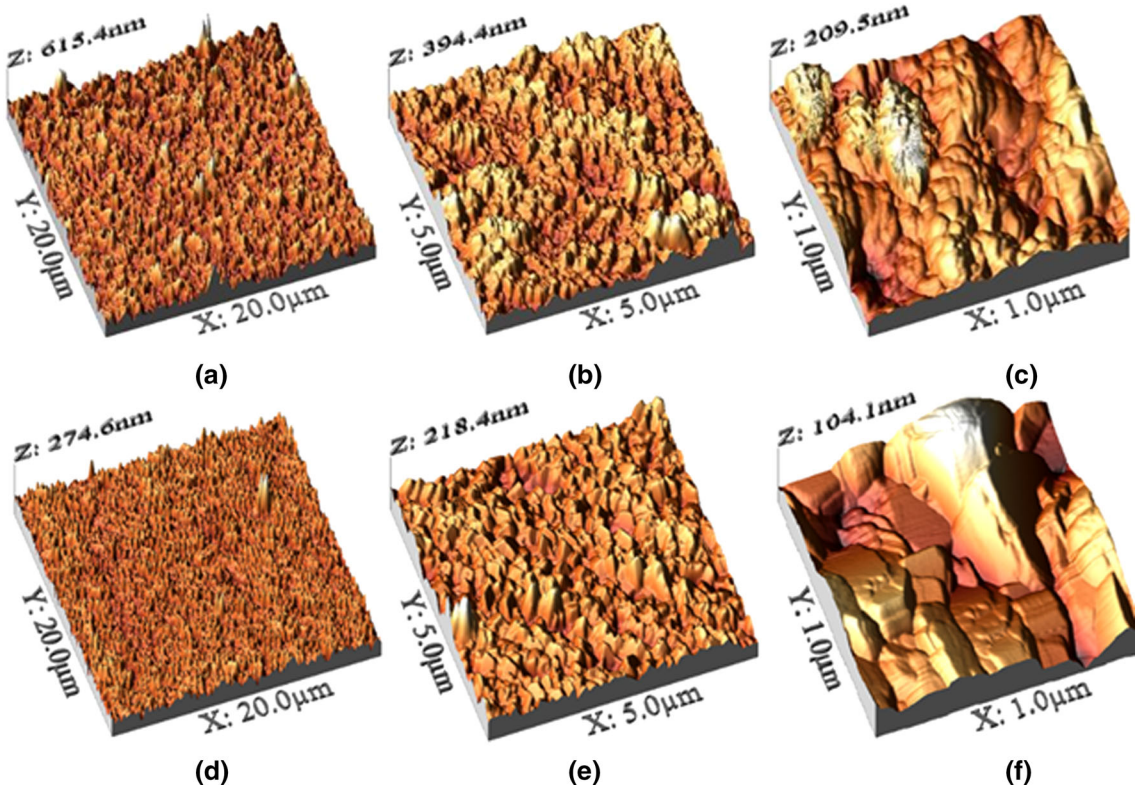

Fig. 3—Topographic AFM image (3-D view) of the oxide layer growth on (*a*) through (*c*) grade 300 and (*d*) through (*f*) grade 350 maraging steels.

Table II. Surface Roughness of the Oxides Produced on Grade 300 and Grade 350 Maraging Steels

Sample	Length (μm)	Roughness Average (R_a) (nm)	Roughness Maximum (R_z) (nm)	Maximum Peak Height (R_p) (nm)	Maximum Depth (R_v) (nm)
Grade 300	20 (Fig. 3(a))	43 ± 0.5	615	421	− 194
	5 (Fig. 3(b))	36 ± 0.5	394	241	− 153
	1 (Fig. 3(c))	24 ± 0.3	209	122	− 87
Grade 350	20 (Fig. 3(d))	15 ± 0.5	274	193	− 82
	5 (Fig. 3(e))	14 ± 0.4	218	138	− 80
	1 (Fig. 3(f))	15 ± 0.3	104	60	− 43

on the surfaces of the samples were determined taking into account the sensitivity factor of the corresponding area for the different measured spectral regions.

A Phenom XL Desktop SEM microscope (Thermo Fisher Scientific, Lenexa, KS, USA) with EDS detector was used to observe the oxide and obtain its chemical composition. Furthermore, the oxide layer thicknesses, as well as their microstructures, were determined by focused ion beam (FIB) milling of cross sections and scanning electron microscopy (SEM) inspection, which was done by using a dual beam workstation Zeiss Neon 40 (Carl Zeiss NTS GmbH, Oberkochen, Germany).

Nanoscratch tests were made with a Nanoindenter XP (MTS) (Nanomechanics, Inc., Oak Ridge, TN, USA), which allows lateral force measurements. A Berkovich indenter was used to scratch the surface under increasing load at a velocity of 10 μm/s, for a total scratch length of 500 μm, up to a maximum load of 100 mN. Three different scratches were performed on each sample. The distance between scratches was held constant and equal to 500 μm to avoid any overlapping effect. The scratch marks were observed using a Phenom XL Desktop SEM microscope (Thermo Fisher Scientific, Lenexa, KS, USA).

III. RESULTS AND DISCUSSION

The oxide layer of all samples was observed and analyzed using different techniques. With laser scanning confocal microscopy (LSCM), several heterogeneities were found distributed along the oxide layer, such as cracks, ridges, peeling, and valleys. In Figure 2, it is possible to appreciate some peeling and cracks on the oxide surface. According to Florez *et al.*,[18] these kinds of defects may be related to the volumetric differences between the different phases forming the oxide layer as well as to the steam condensation on the surface.

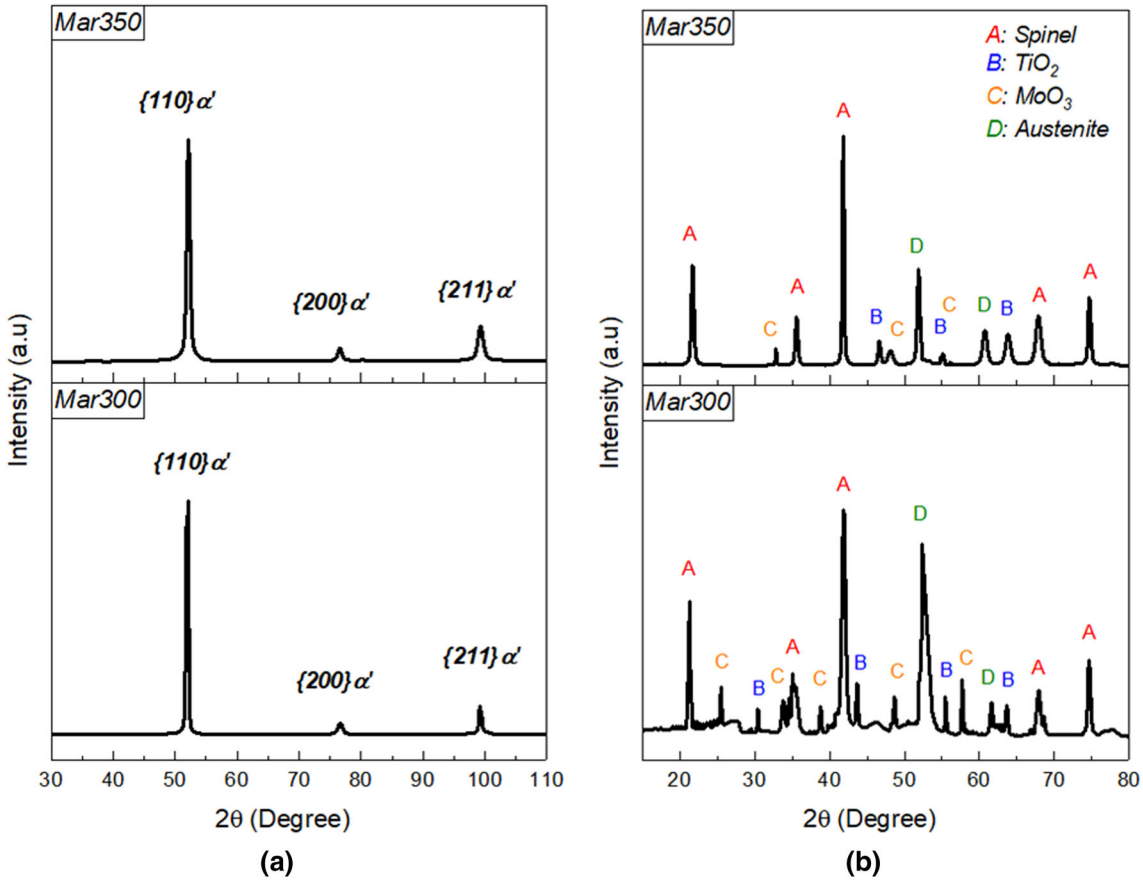

Fig. 4—X-ray diffractograms of the (*a*) solution-annealed state and (*b*) oxide layers produced on both maraging steels.

Figure 3 shows AFM three-dimensional (3-D) topographic images (20 × 20 μm^2, 5 × 5 μm^2, and 1 × 1 μm^2) of the surface quality of the oxide produced on grade 300 (Figures 3(a) through (c)) and on grade 350 too (Figures 3(d) through (f)). From these images, it was possible to directly extract the main roughness parameters (*i.e.*, maximum roughness and maximum and minimum roughness peaks; R_z, R_p, and R_y, respectively), as summarized in Table II. Several different microstructural features (porosity, picks, valleys, *etc.*) are clearly visible, heterogeneously distributed along the surface. With the observation of these images and the analysis of the values in Table II, it is evident that the oxide layer growth on 300 maraging steel grade grows more heterogeneously, in a nonuniform way, and with higher roughness than on grade 350.

X-ray diffractograms before oxidation and the oxide film produced in both steels are shown in Figure 4. Specifically, in Figure 4(a), diffractograms of the samples annealed at 1113.15 K (840 °C) for 1 hour are given and it is possible to identify the peaks (110), (200), and (211), which correspond to the martensitic (α′) phase, in fair agreement with other works.[18,25,26] Figure 4(b) resembles the diffractograms of the oxide layers for both steels. In the two oxides, the same phases, labeled A, B, C, and D, were identified. Peaks correspond to a spinel ferrite, which may be iron, cobalt, nickel, or a mixture of them, according to References 18, 27, 28. On the other hand, it was not possible to determine which types of spinel are formed because they have the same crystallographic structure and lattice parameters.[14,18] The peaks labeled B correspond to TiO_2,[27] while C peaks relate to molybdenum oxide (MoO_3).[27,29] Finally, D peaks match the austenite phase γ,[26] rich in Ni, Fe, and Co, and formed due to the oxidation process at the metal/oxide interface.[14–18]

Therefore, the quantification of the phases in the oxides led to the following results: Oxide formed on maraging 300 is constituted of around 86 pct spinel, 8 pct MoO_3, and 6 pct TiO_2. In the case of the oxide produced on grade 350, the approximate composition was 87 pct spinel, 5 pct MoO_3, and 8 pct TiO_2. It is important to highlight that the spinel peaks present in the XRD diffractograms also fit with Fe_3O_4, $NiFe_2O_4$, and $CoFe_2O_4$, which have similar crystallographic parameters. However, this technique does not lead to

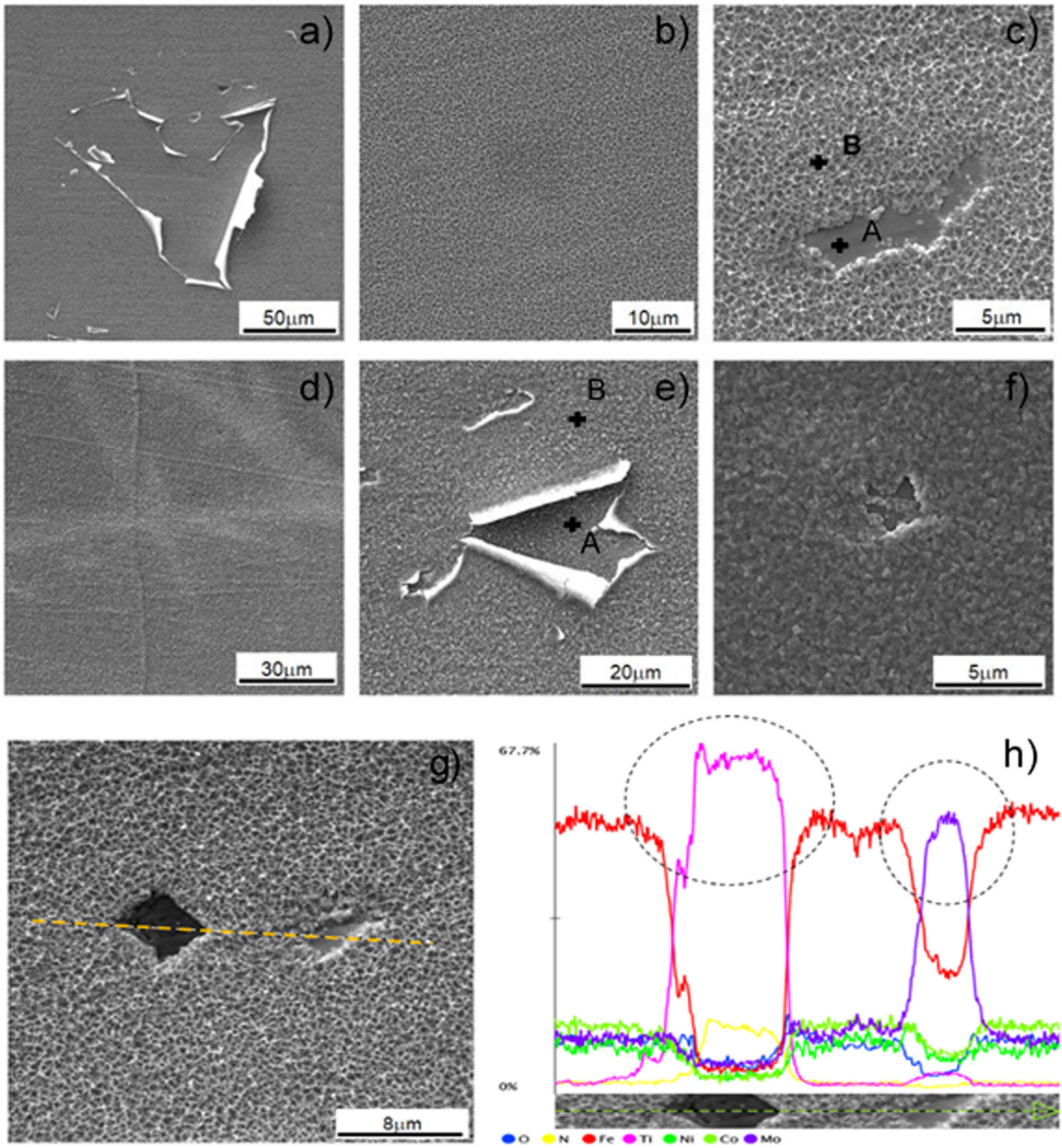

Fig. 5—SEM micrographs of the oxide formed on (*a*) through (*c*) grade 300 and (*d*) through (*g*) grade 350 maraging steels; (*h*) linear EDS spectrum of the oxide formed on grade 300 maraging steel.

isolating each contribution, as reported Klein *et al.*[14] The high percentage of spinel, together with the absence of hematite peaks, shows the effectiveness of the conditions chosen in the procedure to form spinel oxide in these steels. The higher amount of TiO_2 found in the oxide of maraging 350 can be explained by the higher amount of this element in its chemical composition. According to the work of Klein *et al.*,[16] titanium has a greater reactivity than the other elements under these treatment conditions (steam atmosphere at 758.15 K (485 °C)), given the most negative values of free formation energy (ΔF) of Ti oxide (–204 kcal) compared to Fe

(–142 kcal) and Mo oxide (–121 kcal). Moreover, this increase in titanium and its greater reactivity results in a lower amount of molybdenum oxide being found, and this decrease cannot be associated with the amount of molybdenum because Mo content is almost identical in both steels.

The oxide layer morphology from both maraging steels, as observed by SEM, is illustrated in Figures 5 ((a) through (c) grade 300 and (d) through (g) grade 350). Several heterogeneities and defects are visible. Thus, a surface completely covered with several heterogeneities, including holes and peeling, is shown in Figure 5(a). In Figure 5(b), numerous porosities are observed over the entire oxide surface. In Figure 5(c), porosities are observed in more detail as well as an area not covered with external oxide. Then, points highlighted with letters A and B identify the positions where the chemical analyses by EDS were performed. The results summarized in Table III highlight a chemical composition difference: The inner part of the oxide is richer in nickel, titanium, and molybdenum, while the upper part is mainly rich in iron and cobalt. Figure 5(d) shows a covered oxide surface area without defects. Differently dispersed heterogeneities, such as cracks, holes, ridges, valleys, and peeling showing the internal oxide, are observed in Figure 5(e). Punctual EDS analysis was also carried out on the external surface and the internal oxide exposed by the peeling, the results of which are summarized in Table IV. As depicted in this table, the differences between the chemical composition at points A and B show that the inner part of the oxide is richer in alloying elements than the oxide surface, confirming a different concentration in the different parts of the oxide layer. This fact can indicate the existence of different phases or compounds dispersed along with the oxide layer thickness. Finally, in Figure 5(g), linear energy-dispersive X-ray spectroscopy (EDS) was performed following the yellow dash line, in order to compare from the chemical point of view the two holes with the internal area exposed (A and B) and the external zone of the oxide layer. As shown in Figure 5(h), the EDS spectra conducted inside a rectangular hole shape (point A) with straight edges present a chemical composition rich in titanium and nitrogen, which may be related to the formation of titanium nitride (TiN) during the solidification process of steels with an appreciable content of titanium, in accordance with results previously reported by Capurro and Cicutti[30] and Silva *et al.*[31] The EDS spectrum of the irregular hole (point B) indicates that it is rich in molybdenum due to the intermetallic compounds (Ni_3Mo and Fe_3Mo) that precipitate during the aging treatment, as reported in References 1, 3, 18, 32–34. It is essential to indicate that oxygen was only taken into account for comparative purposes.

Fig. 6—SEM micrographs of the oxide layer formed on maraging 300 steel: (*a*) FIB cross-sectional micrograph of the oxide layer, (*b*) thickness of the oxide layer, (*c*) magnification of the oxide layer showing a yellow line where the chemical composition was determined, and (*d*) EDS chemical element profiles conducted on the yellow line of (c) (Color figure online).

Table III. EDS Spot Measurements Taken at the Different Locations Shown in Fig. 5(c)

EDS Quantitative Analysis from A and B Points			
Element Number	Element Symbol	Point A (Weight Concentration)	Point B (Weight Concentration)
26	Fe	47.18	56.67
8	O	23.11	27.36
27	Co	4.84	6.12
28	Ni	7.42	5.55
42	Mo	14.68	3.80
22	Ti	2.77	0.50

Table IV. EDS Spot Measurements Taken at the Different Locations Shown in Fig. 5(e)

EDS Quantitative Analysis from A and B Points			
Element Number	Element Symbol	Point A (Weight Concentration)	Point B (Weight Concentration)
26	Fe	52.06	59.53
8	O	26.01	34.37
27	Co	6.54	4.80
28	Ni	6.56	0.62
42	Mo	7.56	0.58
22	Ti	1.27	0.10

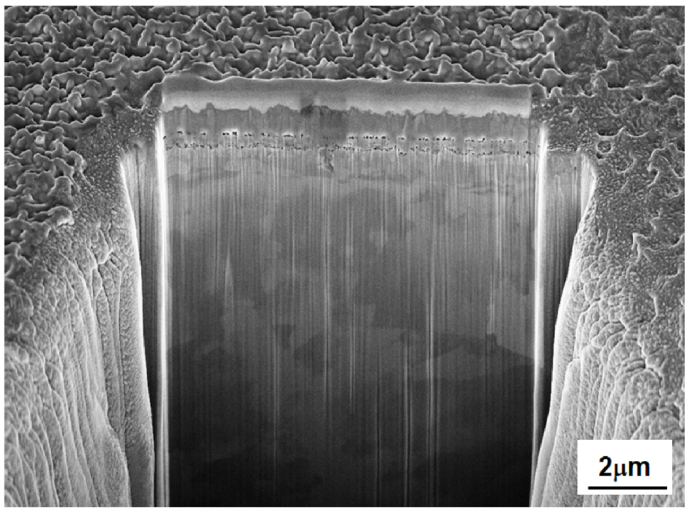
2μm

(a)

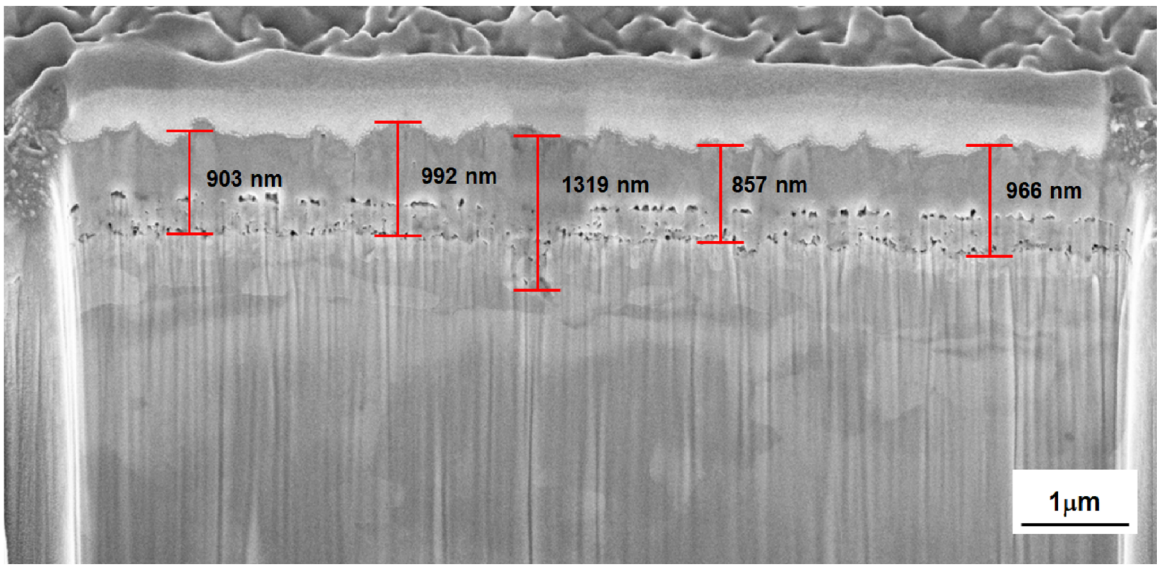
903 nm
992 nm
1319 nm
857 nm
966 nm
1μm

(b)

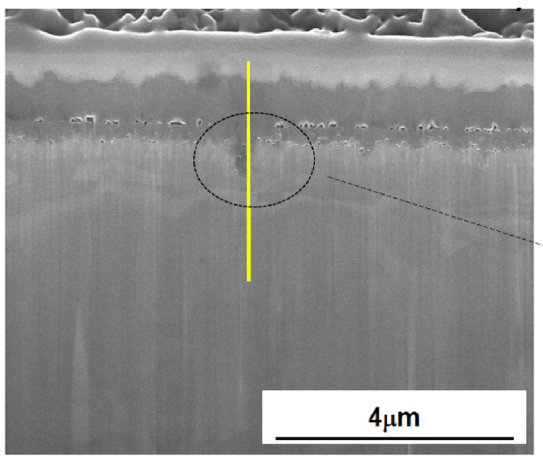
4μm

(c)

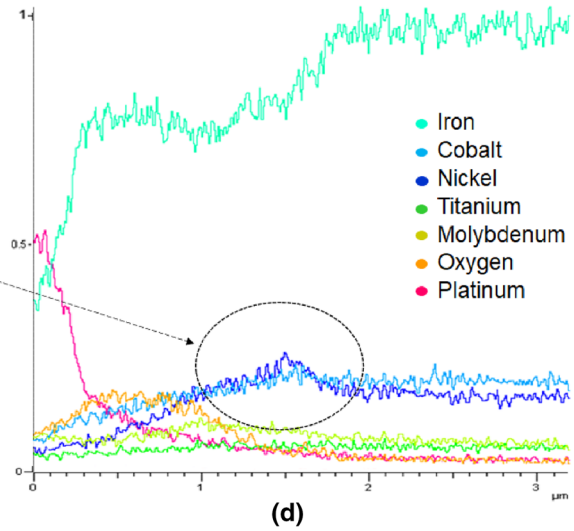
Iron
Cobalt
Nickel
Titanium
Molybdenum
Oxygen
Platinum
1
0.5
0
0
1
2
3
μm

(d)

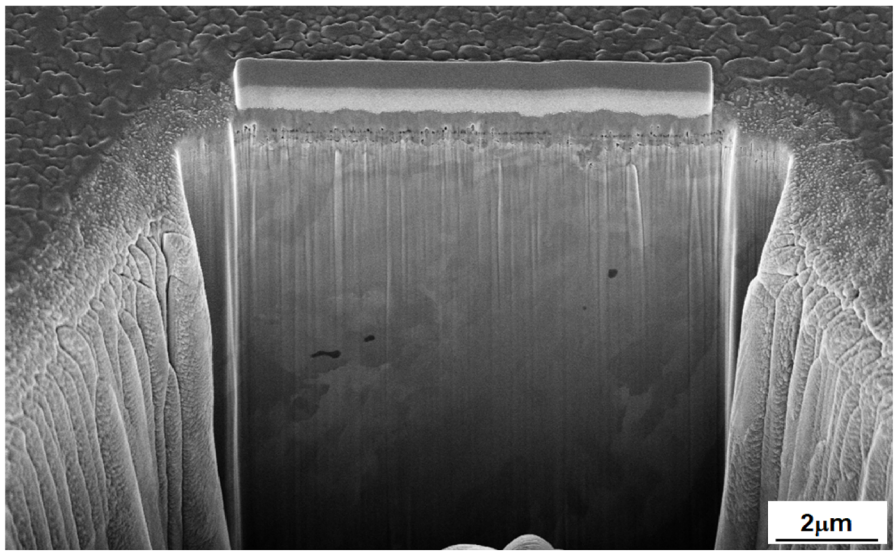
2μm

(a)

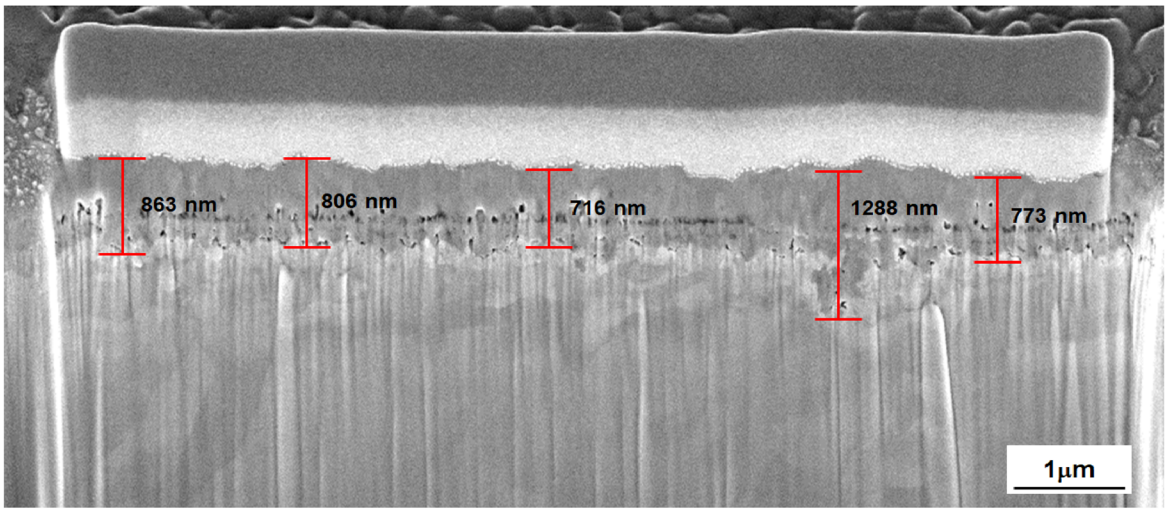
863 nm
806 nm
716 nm
1288 nm
773 nm
1μm

(b)

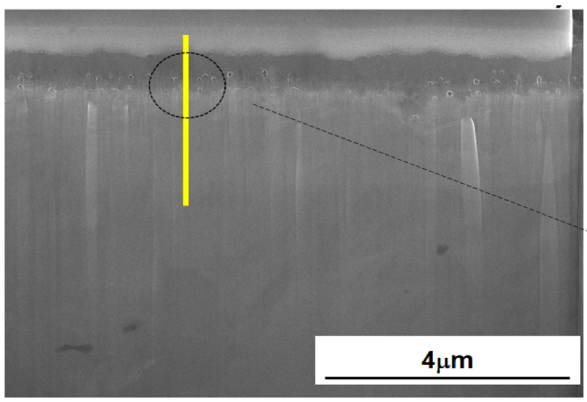
4μm

(c)

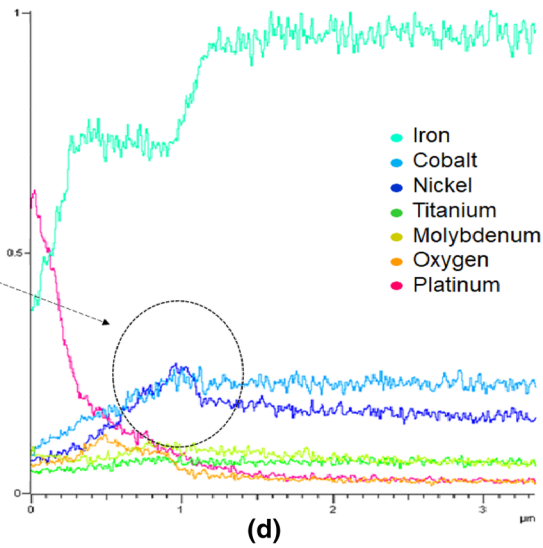
Iron
Cobalt
Nickel
Titanium
Molybdenum
Oxygen
Platinum
1
0.5
0
0
1
2
3
μm

(d)

◀Fig. 7—SEM micrographs of the oxide layer formed on maraging 350 steel: (*a*) FIB cross-sectional micrograph of the oxide layer, (*b*) thickness of the oxide layer, (*c*) magnification of the oxide layer showing a yellow line where the chemical composition was determined, and (*d*) EDS chemical element profiles conducted on the yellow line of (c) (Color figure online).

In order to observe and determine the thickness of the oxides produced on both maraging steels, cross-sectional micrographs were done using FIB. In Figure 6(a), it is possible to observe the platinum plate (used for protection during the assay), the oxide layer, and the steel matrix through the cross section on the oxide produced on maraging steel grade 300. On the other hand, the micrograph in Figure 6(b) shows a homogeneous oxide layer with a thickness ranging between 857 and 1319 nm and a medium thickness around 1007 ± 125 nm. The oxide film presents an irregular outer surface with a series of porelike defects on the internal parts. A closer inspection (Figure 6(c)) shows the oxide layer with a uniform dark shade that suggests no variations of the phases; also, a lighter shade with small grain size is observed on the steel side of the metal-oxide interphase, which could indicate the presence of a different phase from the rest of the metallic matrix of the steel. This assumption was confirmed by performing the linear EDS chemical analysis (Figure 6(d)) in the yellow line in Figure 6(c). It is essential to indicate that oxygen was only taken into account for comparative purposes. These EDS analyses highlight that the oxidized layer presents a uniform distribution from a chemical point of view. In Figure 6(d), it is evident that Co and Ni present a higher concentration in the oxide layer near the metal base interface (specifically in the dash black circles in both figures). This result shows the presence of an austenitic bonding layer rich in nickel, cobalt, and iron at the oxide layer/metal base interface formed during the oxidation process[14–18] and found by XRD analysis made on the samples.

A cross section of the oxide produced on maraging steel grade 350 is observed in Figure 7(a). The micrography in Figure 7(b) shows similar defects (irregular outer surface and with a series of porelike defects on the internal parts) to those found in Figure 6(b) and a homogeneous oxide layer with a thickness ranging between 716 and 1288 nm and medium thickness around 889 ± 160 nm. The closer inspection in Figure 7(c) shows a uniform dark shade on the oxide film and a lighter shade on the steel side of the metal-oxide interphase. The linear EDS chemical analysis (Figure 7(d)) performed in the yellow line in Figure 7(c) confirms a chemical uniform distribution on the oxide and, as found in the oxide produced on maraging steel grade 300, a higher concentration of Co and Ni at the metal-oxide interface (in the areas with dashed black circles in both figures). This result confirms the formation of an austenite phase rich in Ni, Co, and Fe in the metal-oxide interface during the oxidation process and found by XRD analysis. It is essential to indicate that oxygen was only taken into account for comparative purposes.

For the identification of spinel types formed in the oxides of both steels, Raman spectroscopy and XPS techniques were used. Figure 8(a) shows the Raman spectrum obtained from the oxide layers, in which it is possible to see two spinels: iron ferrite (Fe_3O_4)[18,35,36] labeled A and cobalt ferrite ($CoFe_2O_4$)[18,37–39] labeled B. Furthermore, by magnifying a Raman shift ranging between 150 and 750 cm^{-1} (Figure 8(b)), spinel peaks are more clearly visible and the bands for each compound are more detailed. These results confirm the existence of all expected spinels. No hematite bands were detected, confirming the effectiveness of the heat treatment since this compound should be located in the outer layers of the oxide.[18,40–42] These results are in agreement with the XRD finding. Raman spectroscopy did not find MoO_3 and TiO_2 because these compounds are in the innermost layers and this technique analyzes the outermost layers of the oxide.[18]

Figure 9 shows the survey and the high-resolution (b) C 1*s*, (c) O 1*s*, and (d) Fe 2*p* core-level XPS spectra of the oxide produced on maraging steel 300 before and after sputtering for 5 minutes with Ar^+ plasma. In the survey XPS shown in Figure 9(a), it is possible to see the signals of the elements iron (Fe 2*p*), carbon (C 1*s*), cobalt (Co 2*p*), and oxygen (O 1*s*). After etching, the intensity of the C 1*s* signal decreased and the intensities of the other element signals increased. Tables V and VI include the binding energy values (in eV) of the studied signals and the surface chemical composition (in atomic concentration percent), respectively. The C 1*s* core-level spectrum can be decomposed into two contributions in Figure 9(b) (Table V). The main contribution at 284.8 eV is assigned to adventitious carbon, while the other contribution at 285.7 eV is derived from the presence of C-O bonds.[18,43,44] After etching 5 minutes, there are only two contributions at 284.8 and 285.9 eV, and the surface concentration of C decreased from 48.1 to 1.6 pct (Table VI), being indicative, as expected, of adventitious contamination, which is very common on the surface of metals. The assignment of the oxygen species in the O 1*s* signal is not easy. The O 1*s* signal in Figure 9(c) can be decomposed into three contributions at 529.9, 531.2, and 532.2 eV. The first one, denoted Oα, can be related to the presence of surface lattice oxygen (O^{2-}), whereas the contribution at 531.2 eV, denoted Oβ, is assigned to the presence of defect oxide or to surface low coordination oxygen ion. The third contribution mainly proceeds from hydroxyl groups and C-O groups. After etching 5 minutes, the relative intensity of the contribution due to lattice oxygen increased. In fact, the oxygen surface content slightly increased after etching from 36.3 to 45.1 pct (Table VI).[18,45,46]

The Fe 2*p* core-level spectra of the oxide produced on maraging 300 before and after etching 5 minutes with Ar^+ are shown in Figure 9(d), where the deconvolution of the Fe $2p_{3/2}$ signal is also included, and the corresponding values of the different contributions are shown in Table V. It is well known that the positions of the

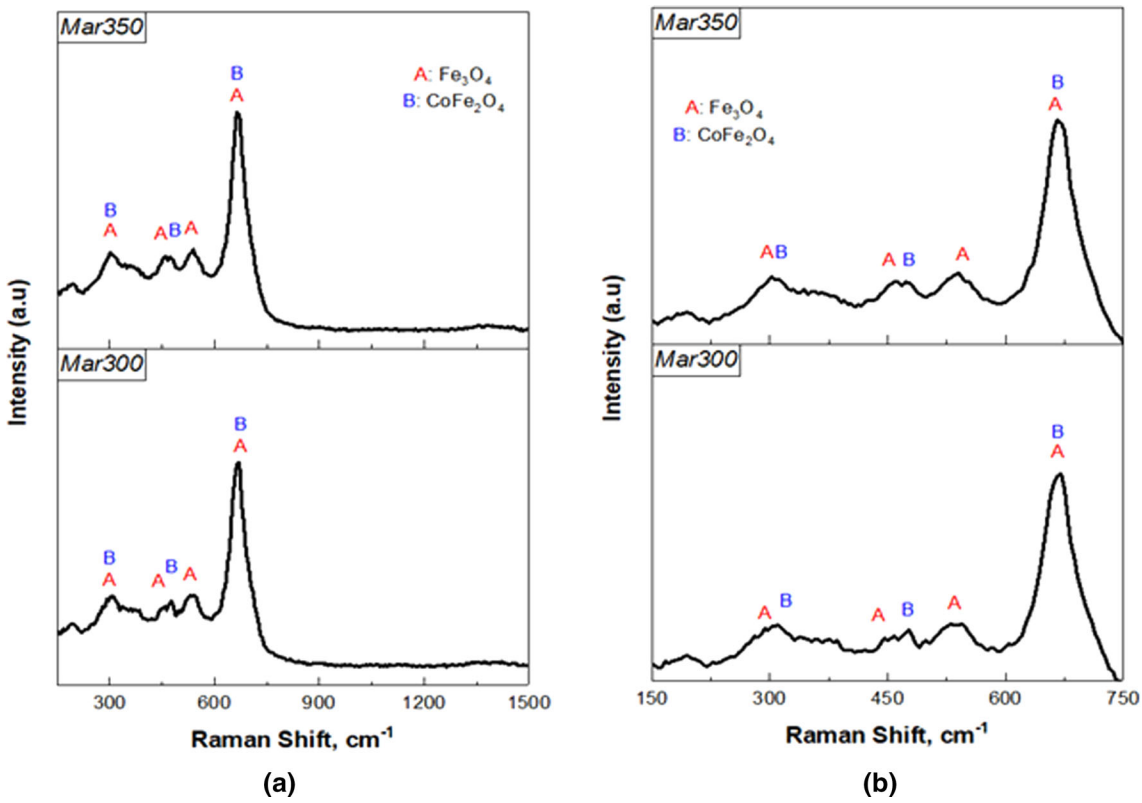

Fig. 8—Raman spectra of oxides produced on the maraging steels investigated here.

contributions of the Fe $2p_{3/2}$ signal, as well as its satellite peak, are very sensitive to the oxidation state of iron.[18,47–49] It is clear that the etching process modifies the Fe $2p$ signal. Upon etching, the intensity of the signal increased and the surface iron content went from 10.4 to 35.4 pct in atomic concentration (Table VI). The deconvolution of the Fe $2p_{3/2}$ main peak is also shown in Figure 9(e). This peak is deconvoluted in three contributions at 708.1 to 709.8 eV assigned to Fe^{2+}, 710.3 to 711.3 eV assigned to Fe^{3+}, and 712.1 to 712.7 eV related to an interaction of Fe^{2+} and Fe^{3+}.[50] The decrease in the $Fe^{2+}/(Fe^{2+} + Fe^{3+})$ ratio after etching can be associated with a greater amount of magnetite in the most external areas. Fe_3O_4 contains the iron ions Fe^{2+} and Fe^{3+}. While the increase in the Fe^{3+} ratio after etching (Table V), and the consequent decrease in the Fe^{2+} ratio, would indicate the formation of another type of spinel ferrites, such as the cobalt ferrite ($CoFe_2O_4$), this valuation is consistent with the highest amount of cobalt after etching (Table VI), remembering that in this compound iron and cobalt ions have the oxidation states Fe^{3+} and Co^{2+}, respectively. It is also important to mention that the Fe/Co atomic ratio is 35.4/17.9 = 1.99, very close to the theoretical value for the cobalt spinel $CoFe_2O_4$.[51–56] All these results agree with the literature,[18,28,40,57–60] where the diffusion of Co and Ni ions, in the form of Co^{2+} and Ni^{2+} species, from the metallic matrix to the outside is explained.

The Co $2p$ core level spectra (not shown) are very complex. The Co $2p$ spectrum before etching shows a maximum at 784.0 eV assigned to Co^{2+}, but this assignment is difficult because the presence of Co^{3+} species cannot be ruled out. Upon etching, two maxima are observed at 780.7 and 786.0 eV. The new contribution at low binding energy is assigned to reduced Co species.[52–56]

Figure 10 shows the survey spectra and the high-resolution (b) C 1*s*, (c) O 1*s*, and (d) Fe $2p$ core level XPS spectra of the oxide produced on maraging steel 350, before and after sputtering for 5 minutes with Ar^+ plasma. In the survey shown in Figure 10(a), the signals of iron (Fe $2p$), carbon (C 1*s*), cobalt (Co $2p$), and oxygen (O 1*s*) are discerned. After etching, the intensity of the adventitious carbon signal decreased and, as expected, the relative intensities of the other studied elements increased. Tables V and VI show the binding energy values (in eV) of the studied signals and the surface chemical composition, respectively. The C 1*s* high-resolution spectrum was similar to that observed in the case of the oxide produced on maraging 300. The C

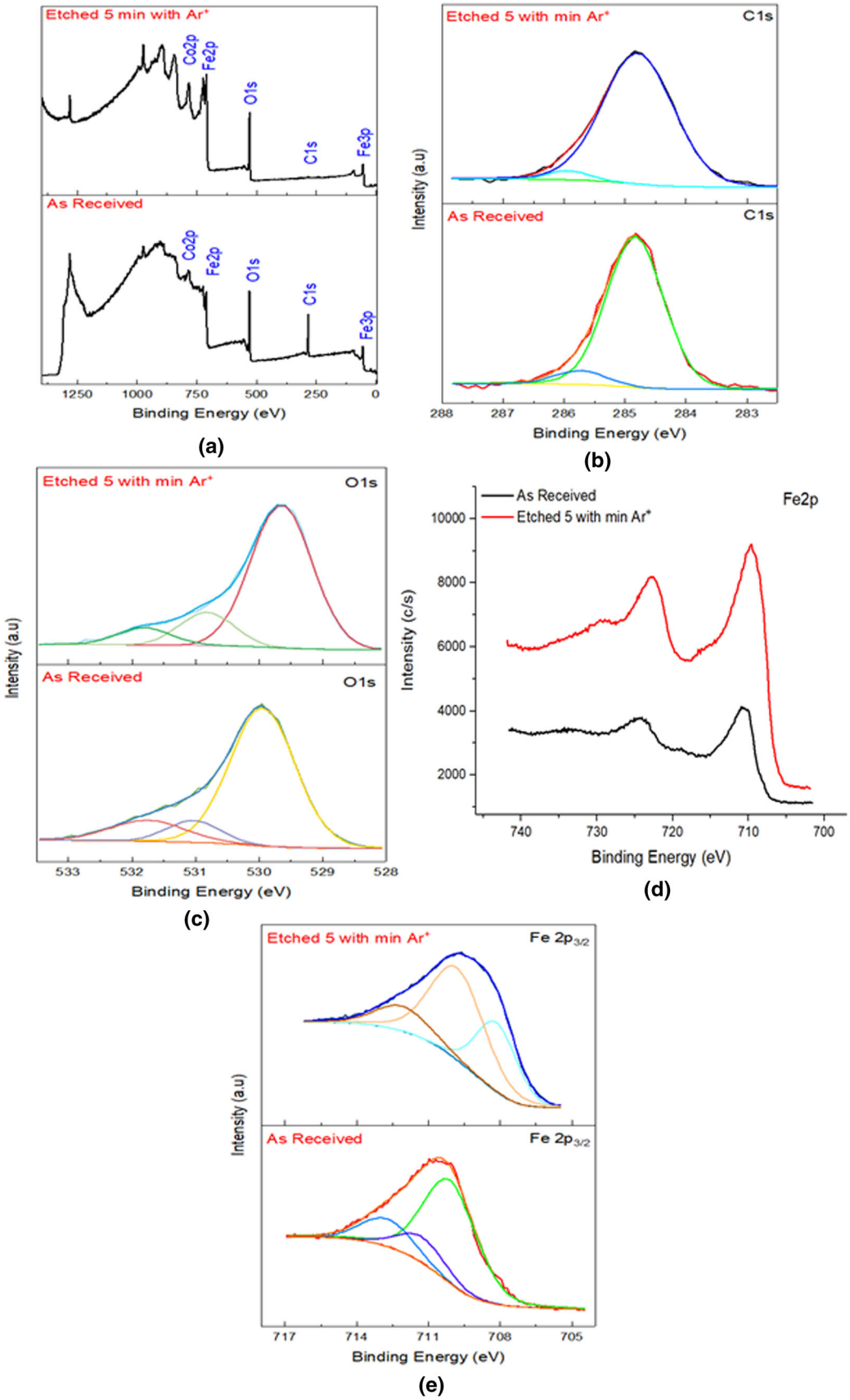

Fig. 9—XPS spectra of the oxide formed on maraging steel 300 before (as received) and after etching 5 min with Ar^+ plasma (etched 5 min Ar^+): (*a*) survey spectrum, (*b*) C 1*s*, (*c*) O 1*s*, (*d*) Fe 2*p*, and (*e*) Fe $2p_{3/2}$ deconvoluted.

Table V. Binding Energy Values (in eV) of the Studied Elements and Percentages of Relative Area in Brackets and $Fe^{2+}/(Fe^{2+} + Fe^{3+})$ Ratios for the Studied Oxide Produced on Maraging Steels before and after Etching 5 Minutes With Ar^+ Plasma

Sample	C 1*s*	O 1*s*	Fe $2p_{3/2}$	Co $2p_{3/2}$	$Fe^{2+}/(Fe^{2+}+Fe^{3+})$
Mar300	284.8 (92)	529.9 (76)	709.8 (68)	784.0	68
	285.7 (8)	531.0 (10)	711.3 (15)		
		531.8 (14)	712.7 (17)		
Mar300 After 5 min Ar^+	284.8 (96)	529.6 (76)	708.1 (29)	780.7	29
	285.9 (4)	530.8 (15)	710.3 (56)	786.0	
		531.8 (9)	712.1 (15)		
Mar350	284.8 (96)	529.9 (80)	710.1 (68)	784.2	68
	285.6 (4)	531.1 (12)	711.8 (28)		
		532.0 (8)	713.6 (4)		
Ma350 After 5 min Ar^+	284.8 (93)	529.7 (78)	708.0 (14)	782.6	14
	285.8 (7)	531.0 (18)	709.4 (68)	788.4	
		532.2 (3)	712.4 (25)		

Table VI. Surface Chemical Composition (Atomic Percent) for the Studied Oxide Produced on Grade 300 and Grade 350 Maraging Steels Before and After Etching 5 Minutes With Ar^+ Plasma

Sample	C	O	Fe	Co
Mar300	48.1	36.3	10.4	5.3
Mar300 After 5 min Ar^+	1.6	45.1	35.4	17.8
Mar350	42.6	38.6	11.5	7.6
Mar350 After 5 min Ar+	3.9	49.3	31.6	15.2

1*s* core-level spectrum was decomposed into two contributions in Figure 10(b) (Table V). The O 1*s* core level spectra also show three contributions (Figure 10(c) and Table V) at 529.9, 531.1, and 532.0 eV, but in this case, the surface content of the O 1*s* core level is higher compared to that observed for grade 300. The Fe 2*p* core-level spectra for the oxide produced on maraging 350 are shown in Figure 10(d), where the difference between both core level intensities (before and after etching) is appreciable, being lower than for grade 300. However, iron content increased upon etching, from 11.5 to 31.6 pct (Table VI). The Fe 2p core-level spectrum for the etched oxide produced on maraging steel 350 is different, with a much lower relative intensity of the contribution at 708.0 eV assigned to Fe^{2+}. This fact points out that before etching this sample presented a high concentration of the iron spinel Fe_3O_4, with higher concentration of Fe^{2+}. After etching, the $Fe^{2+}/(Fe^{2+} + Fe^{3+})$ ratio decreased to 14, and taking into account the fact that the Fe/Co atomic ratio is 36.64/18.14 = 2.07, a value very near the theoretical one for the cobalt spinel $CoFe_2O_4$ (formed by the metal ions Fe^{3+} and Co^{2+}), and that in the innermost areas of the oxide there is a greater concentration of cobalt (Table VI), it is feasible to have a greater quantity of the cobalt spinel $CoFe_2O_4$.

The Co 2*p* core spectrum after etching shows two maxima at 780.7 and 782.7 eV, with a difficult assignment but indicating the presence of Co^{2+} and Co^{3+}. The possible formation of a cobalt spinel Co_3O_4 cannot be discarded, together with the presence of the spinel $CoFe_2O_4$.

In order to determine the adhesive damage between the former oxide layer and the different metallic maraging alloy substrates, also denoted as Pc_2, scratch tests were conducted at the submicrometric length scale in order to confine the deformation stress field at the coating/substrate interface. Figure 11 (left-hand side) shows the entire scratch track for both investigated systems in order to qualitatively observe the induced damage along the sliding track. Figure 11 (right-hand side) shows the top-view SEM micrograph of nano-scratch tracks, where some interesting features are clearly visible—mainly cracks at the edge of the sliding track and subsequently chipping of the former oxide layer. The Pc_2 values directly determined from the SEM micrographs are summarized in Table VII. From Figure 11 and the Pc_2 summarized in Table VII, it is clearly visible that the oxide layer grown on the maraging 300 alloy required a higher sliding force in order to detach the oxide layer growth under N_2 atmosphere from the metallic maraging substrate. However, both oxide films present good adherence, and the results show the capability for their use for tribological applications under sliding contact tests.[18]

The preceding results illustrate several similarities between the oxides produced in both steels. They have the same superficial defects, although the oxide on grade 300 is slightly rougher than that on the 350 maraging

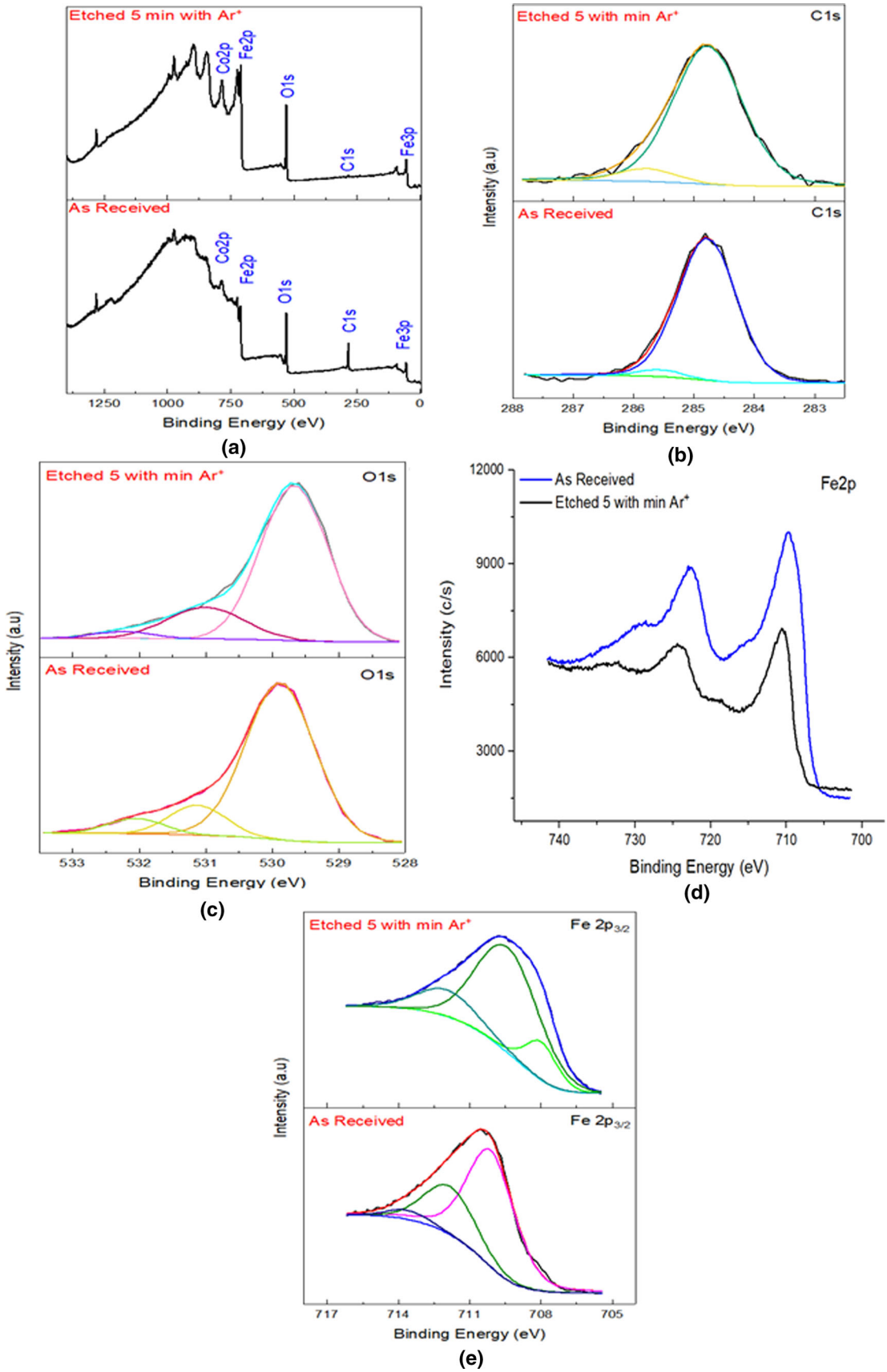

Fig. 10—XPS spectra of the oxide formed on maraging steel 350 before (as received) and after etching 5 min with Ar^+ plasma (etched 5 min Ar^+): (*a*) survey spectrum, (*b*) C 1*s*, (*c*) O 1*s*, (*d*) Fe 2*p*, and (*e*) Fe $2p_{3/2}$ deconvoluted.

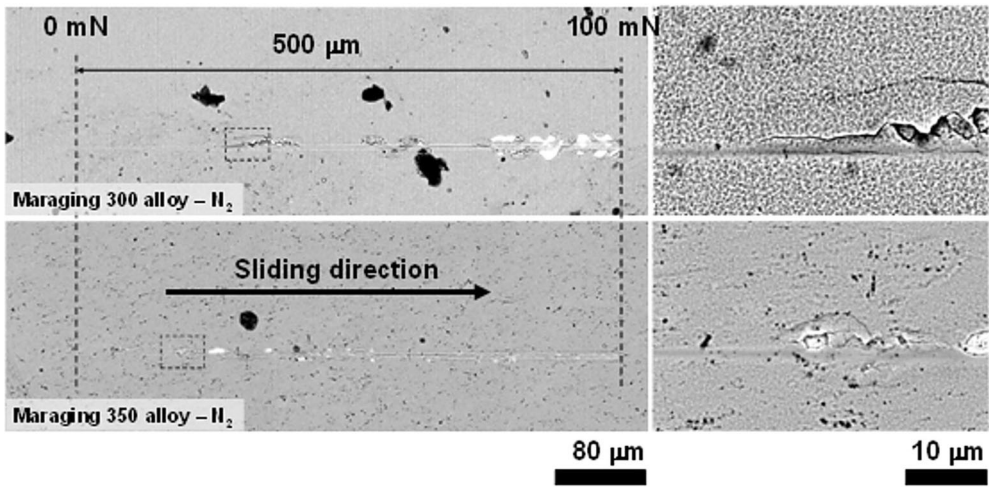

Fig. 11—SEM micrograph for the nanoscratch track (left) and magnification of the top-view SEM micrographs of nanoscratch tracks where the first adhesive damage appears (right).

Table VII. Pc_2 Directly Determined From the SEM Micrographs for Each Oxide Produced on Each Maraging Steel

Steel Where the Oxide was Formed	Pc_2 (mN)
Mar300	32
Mar350	16

steel. These differences may not be associated with the chemical composition of the oxide (similar for both) or to the previous sample roughness (the same for both).

Molybdenum (MoO_3) and titanium (TiO_2) oxides were found in the internal layers of the oxide, with higher quantities in the innermost part of the film. For this reason, they were not detected by Raman spectroscopy and XPS. These results are in accordance with References 16, 18, 41, 61 which explain how these types of compounds are formed in the initial stages of the oxidation process and are only found in the inner parts of the oxide because iron oxides, which have greater growth kinetics, cover molybdenum and titanium oxides.

Thermodynamic and kinetic stability conditions allow the iron oxide Fe_3O_4 to be formed during the growth process of the oxide layer, as mentioned in References 14–17, 41, 61–64. However, from these same conditions, elements, such as cobalt and nickel, can also diffuse within the oxide. Klein *et al.*[14–16] mentioned that it is possible to find these elements within the iron spinel as substitutes but not as another compound. In this work, as well as in Reference 18, it was observed that these elements form a mixture of spinels: $CoFe_2O_4$, $NiFe_2O_4$, and Fe_3O_4. The formation of this spinel mixture is possible by the diffusion reaction of Co^{2+} and Ni^{2+} from the metallic matrix to the outside of the oxide. Then, the diffusion of these ions replaces Fe^{2+} ions in the octahedral sites of spinel and in the external part of the film, where they form Fe_3O_4. In the present case, the high cobalt content of maraging steels, and also the formation of nickel-rich austenite in the oxide layer/metal interface (due to the decomposition of martensite at temperatures near 773.15 K (500 °C)), influences the preferential formation of the cobalt ferrite spinel.[10,18,28,40,57–60]

It is possible that in the innermost layers, where there is more nickel, spinel $NiFe_2O_4$ was formed, but it was not detected in the upper layers. Also, the gradient of composition of cobalt observed in the results of EDS and XPS, where a greater quantity is observed in the innermost layers, confirms that the spinel $CoFe_2O_4$ has a bigger amount in the internal regions of the oxide.

The conditions of time and temperature in the present procedure, as well as the steps using nitrogen (without available oxygen) and focusing on the oxidation process taking place only with steam, allowed the formation of a spinel-like oxide film. Hematite was not found due to an oxygen deficit during the heat treatment, an indispensable factor for the transformation of magnetite (Fe_3O_4) into hematite (α-Fe_2O_3) to occur on the outer part of the oxide under the temperature conditions used in the procedure.[18,40–42,63–66]

IV. CONCLUSIONS

A chemical composition gradient from the innermost toward the external surface of the oxide was observed in both steels, with a higher quantity of alloying elements, such Ni, Ti, Mo, and Co, in the oxide layer/metal

interface. Then, due to the nickel gradient composition in the metal/oxide interphase, the formation of nickel-rich austenite was possible in the steel, and the formation in a great quantity of the nickel spinel ferrite $NiFe_2O_4$ next to this region cannot be discarded.

Another implication of the chemical composition gradient is the formation of molybdenum (MoO_3) and titanium (TiO_2) oxides in the internal layers of the oxide. These compounds are formed in the initial stages of the oxidation process and are only found in the inner parts of the oxide because iron oxides, which have greater growth kinetics, cover molybdenum and titanium oxides.

The thermodynamic and kinetic conditions of the heat treatment investigated here allowed the formation of the iron ferrite spinel Fe_3O_4, and the consequent formation of the spinel mix $NiFe_2O_4$, $CoFe_2O_4$, and Fe_3O_4, by the diffusion reaction of cobalt and nickel ions (Co^{2+} and Ni^{2+}) from the metallic matrix to the outside of the oxide, replacing Fe^{2+} ions in the octahedral sites of the spinel and displacing part of these iron ions to the external part of the film, where they formed Fe_3O_4.

Moreover, the conditions of the heat treatment, specifically the nitrogen atmosphere at the first stage (without available oxygen), allowed the formation of a spinel-like oxide film and avoided the formation of hematite oxide.

The oxides produced in both maraging steels present similar roughness and relatively similar thickness and present the same defects such as porosity, metal-oxide interface, and irregular outer surface. It was also possible to observe in both steels the austenitic phase rich in nickel and cobalt detected by XRD that was formed during the oxidation process at the base of the steels.

The maraging 300 steel presents a good adherence between the formed oxide layer and the metallic substrate growth under the N_2 atmosphere. However, both oxide films demonstrate good adherence and their capability for use under aggressive conditions mainly for tribological applications under sliding contact tests.

ACKNOWLEDGMENTS

The authors gratefully acknowledge the CAPES/PRINT-UFC, FUNCAP, and CNPq for financial assistance. The authors thank the Central Analítica-UFC (funded by Finep-CT-INFRA, CAPES-Pró-Equipamentos, and MCTI-CNPq-SisNano2.0) for microscopy measurements and the Barcelona Research Center in Multiscale Science and Engineering–UPC, CIEFMA-UPC, LACAM-UFC, GPSA-UFC, and NIM-UMA Research Groups for technical support. One of the authors (ERC) thanks Project RTI2018-099668-BC22 of Ministerio de Ciencia, Innovación y Universidades, and Project UMA18-FEDERJA-126 of Junta de Andalucía and FEDER funds. Finally, JJR acknowledges the Serra Hunter Programme of the "Generalitat de Catalunya."

FUNDING

This work was supported by the Coordenação de Aperfeiçoamento de Pessoal de Nível Superior (CAPES) PRINT-88887.371681/2019-00.

AVAILABILITY OF DATA AND MATERIAL (DATA TRANSPARENCY)

Not applicable.

CODE AVAILABILITY

Not applicable.

CONFLICT OF INTEREST

The authors declare that they have no known competing financial interests or personal relationships that could have appeared to influence the work reported in this article.

REFERENCES

1. A. Magnée, J.M. Drapier, J. Dumont, D. Coutsouradis, and L. Habraken: *Cobalt Containing High Strength Steels*, Centre d'Information du Cobalt, Brussels, 1974, p. 128, http://refhub.elsevier.com/S0360-3199(19)31930-5/sref1.
2. M. Schmidt and K. Rohrbach: *ASM Handbook*, ASM International, Materials Park, OH, 1991, vol. 4, pp. 219–28, https://doi.org/10.31399/asm.hb.v04d.a0005948.
3. H.J. Rack and D. Kalish: *Metall. Trans.*, 1971, vol. 2, pp. 2011–20. https://doi.org/10.1007/BF02814948.
4. L.P.M. Santos, M. Bêres, I.N. Bastos, S.S.M. Tavares, H.F.G. Abreu, and M.J.G. Silva: *Corros. Sci.*, 2015, vol. 101, pp. 12–18. https://doi.org/10.1016/j.corsci.2015.06.022.
5. V. LimaFilho, I. Barrosa, and H. Gomes de Abreu: *Mater. Res.*, 2017, vol. 20(1), pp. 10–14. https://doi.org/10.1590/1980-5373-mr-2016-0257.
6. M. Masoumi, H.F.G. Abreu, L.F.G. Herculano, J.M. Pardal, S.S.M. Tavares, and M.J.G. Silva: *Eng. Fail. Anal.*, 2019, vol. 104, pp. 379–87. https://doi.org/10.1016/j.engfailanal.2019.05.031.
7. U.K. Viswanathan, G.K. Dey, and M.K. Asundi: *Metall. Trans. A.*, 1993, vol. 24A, pp. 2429–42. https://doi.org/10.1007/BF02646522.
8. "18 Per Cent Nickel Maraging Steels: Engineering Properties." Nickel Development Institute Report No. 4419, Nickel Institute, 1976, https://nickelinstitute.org/media/1598/18_nickelmaragingsteel_engineeringproperties_4419_.pdf.
9. M.A. Cerra Florez, U.C. Pereira, J.L. Cardoso, F.J.S. Oliveira, W.S. Araújo, G.F. Ribas, H.F.G. De Abreu, and M.J.G. Da Silva: *J. Fluor. Chem.*, 2021, vol. 243, p. 109738. https://doi.org/10.1016/j.jfluchem.2021.109738.
10. M.J.G. Silva, J.L. Cardoso, D.S. Carvalho, L.P.M. Santos, L.F.H. Herculano, H.F.G. Abreu, and J.M. Pardal: *Int. J. Hydrog. Energy.*, 2019, vol. 44, pp. 18606–15. https://doi.org/10.1016/j.ijhydene.2019.05.074.
11. A. Glaser: *Sci. Glob. Secur.*, 2008, vol. 16, pp. 1–25. https://doi.org/10.1080/08929880802335998.
12. I. Barzashka and I. Oelrich: *Engineering Considerations for Gas Centrifuges*, Federation of American Scientists, https://fas.org/programs/ssp/nukes/fuelcycle/centrifuges/engineering.html#14. Accessed 14 March 2020.
13. D.B. Bradhurst and P.M. Heuer: *Corrosion.*, 1981, vol. 37(2), pp. 63–70. https://doi.org/10.5006/1.3593847.
14. I. Klein, J. Sharon, and A. Yaniv: *Scripta Metall.*, 1981, vol. 15, pp. 141–44. https://doi.org/10.1007/BF00666721.

15. I. Klein, A. Yaniv, and J. Sharon: *Oxid. Met.*, 1981, vol. 16, pp. 1–2. https://doi.org/10.1007/BF00603746.
16. I. Klein, A. Yaniv, and J. Sharon: *Appl. Surf. Sci.*, 1983, vol. 14(3–4), pp. 351–58. https://doi.org/10.1016/0378-5963(83)90048-X.
17. J. Rezek, I. Klein, and J. Yahalom: *Appl. Surf. Sci.*, 1997, vol. 108, pp. 159–65. https://doi.org/10.1016/S0169-4332(96)00587-9.
18. M.A.C. Florez, G. Fargasribas, J.J.R. Rovira, E. Vilarrassa-García, E. Rodríguez-Castellón, A.B.F. Souza, J.L. Cardoso, and M.J. Gomes da Silva: *Metals.*, 2021, vol. 11(5), p. 746. https://doi.org/10.3390/met11050746.
19. I. Horcas and R. Fernández: *Rev. Sci. Instrum.*, 2007, vol. 78, p. 013705. https://doi.org/10.1063/1.2432410.
20. Y. Zhang, K. Cui, Q. Gao, S. Hussain, and Y. Lv: *Surf. Coat. Technol.*, 2020, vol. 396, p. 125966. https://doi.org/10.1016/j.surfcoat.2020.125966.
21. U.C. Nwaogu, N.S. Tiedje, and H.N. Hansen: *J. Mater. Process. Technol.*, 2013, vol. 213, pp. 59–68. https://doi.org/10.1016/j.jmatprotec.2012.08.008.
22. E.S. Gadelmawla, M.M. Koura, T.M.A. Maksoud, I.M. Elewa, and H.H. Soliman: *J. Mater. Process. Technol.*, 2002, vol. 123, pp. 133–45. https://doi.org/10.1016/S0924-0136(02)00060-2.
23. F. Chung: *J. Appl. Cryst.*, 1974, vol. 7, p. 519. https://doi.org/10.1107/S0021889874010375.
24. X. Zhou, D. Liu, H. Bu, L. Deng, H. Liu, P. Yuan, P. Du, and H. Song: Solid. *Earth Sci.*, 2018, vol. 3, pp. 16–29. https://doi.org/10.1016/j.sesci.2017.12.002.
25. N.F. Viana, N.C. Dos Santos, and H.F.G. De Abreu: *J. Mater. Res. Technol.*, 2013, vol. 2, pp. 298–302. https://doi.org/10.1016/j.jmrt.2013.03.017.
26. F.F. Conde, J.D. Escobar, J.P. Oliveira, M. Béreš, A.L. Jardini, W.W. Bose, and J.A. Avila: *Mater. Sci. Eng. A.*, 2019, vol. 758, pp. 192–201. https://doi.org/10.1016/j.msea.2019.03.129.
27. JCPDS: "X-ray Diffraction Data Cards of the Joint Committee on Powder Diffraction Standards," International Center for Diffraction Data, Swarthmore, PA, 1975.
28. J. Dąbrowa, M. Stygar, A. Mikuła, A. Knapik, K. Mroczka, W. Tejchman, and M. Martin: *Mater. Lett.*, 2018, vol. 216, pp. 32–36. https://doi.org/10.1016/j.matchar.2007.03.011.
29. N. Zhao, H. Fan, M. Zhang, J. Ma, Z. Du, B. Yan, and H. Li: *Chem. Eng. J.*, 2020, vol. 390, p. 124477. https://doi.org/10.1016/j.cej.2020.124477.
30. C. Capurro and C. Cicutti: *J. Mater. Res. Technol.*, 2018, vol. 7(3), pp. 342–49. https://doi.org/10.1016/j.jmrt.2018.04.010.
31. C.C. Silva, J.P. Farias, H.C. Miranda, R.F. Guimarães, J.W.A. Menezes, and A.M. Neto: *Mater. Charact.*, 2008, vol. 59, pp. 528–33. https://doi.org/10.1016/j.matchar.2007.03.011.
32. E.R. Petty: *J. Appl. Cryst.*, 1970, vol. 4, pp. 402–03. https://doi.org/10.1107/S0021889871007349.
33. A.C. Rodrigues, H.H. Bernardi, and J. Otubo: *J. Aerosp. Technol. Manag.*, 2014, vol. 6(4), pp. 389–94. https://doi.org/10.5028/jatm.v6i4.400.
34. O. Moshka, M. Pinkas, E. Brosh, V. Ezersky, and L. Meshi: *Mater. Sci. Eng. A.*, 2015, vol. 638, pp. 232–39. https://doi.org/10.1016/j.msea.2015.04.067.
35. P.R. Kumar, Y.H. Jung, K.K. Bharathi, C.H. Lim, and D.K. Kim: *Electrochim. Acta.*, 2014, vol. 146, pp. 503–10. https://doi.org/10.1016/j.electacta.2014.09.081.
36. M.R. Robinson, M. Abdelmoula, M. Mallet, and R. Coustel: *J. Solid State Chem.*, 2019, vol. 277, pp. 587–93. https://doi.org/10.1016/j.jssc.2019.06.033.
37. W. Wang, Z. Ding, and X. Zhao: *J. Appl. Phys.*, 2015, vol. 117, p. 17A328. https://doi.org/10.1063/1.4917463.
38. K.L. Routray, S. Saha, and D. Behera: *Mater. Sci. Eng. B.*, 2020, vol. 257, p. 114548. https://doi.org/10.1016/j.mseb.2020.114548.
39. J. De La Figuera, A. Quesada, L. Martín-García, M. Sanz, M. Oujja, E. Rebollar, M. Castillejo, P. Prieto, A. Muñoz-Martín, L. Aballe, and J.F. Marco: *Appl. Surf. Sci.*, 2015, vol. 359, pp. 480–85. https://doi.org/10.1016/j.apsusc.2015.10.104.
40. F. Genuzio, A. Sala, Th. Schmidt, D. Menzel, and H.-J. Freund: *Surf. Sci.*, 2016, vol. 648, pp. 177–87. https://doi.org/10.1016/j.susc.2015.11.016.
41. R. Subbaraman, S.A. Deshmukh, and S.K. Sankaranarayanan: *J. Phys. Chem. C.*, 2013, vol. 117, pp. 5195–5207. https://doi.org/10.1021/jp312514m.
42. X. Zhang, S. Yang, Z. Yang, and X. Xu: *J. Appl. Phys.*, 2016, vol. 120, p. 085313. https://doi.org/10.1063/1.4961607.
43. P. Kaspar, D. Sobola, R. Dallaev, S. Ramazanov, A. Nebojsa, S. Rezaee, and L. Grmela: *Appl. Surf. Sci.*, 2019, vol. 493, pp. 673–78. https://doi.org/10.1016/j.apsusc.2019.07.058.
44. D. Barreca, G.A. Battiston, D. Berto, R. Gerbasi, and E. Tondello: *Surf. Sci. Spectra.*, 2001, vol. 8, p. 240. https://doi.org/10.1116/11.20020302.
45. A. Galtayries, R. Sporken, J. Riga, G. Blanchard, and R. Caudano: *J. Electron Spectrosc.*, 1998, vol. 88, pp. 951–56. https://doi.org/10.1016/S0368-2048(97)00134-5.
46. T.L. Barr: *J. Phys. Chem.*, 1978, vol. 82, pp. 1801–10. https://doi.org/10.1021/j100505a006.
47. A.P. Grosvenor, B.A. Kobe, M.C. Biesinger, and N.S. McIntyre: *Surf. Interface Anal.*, 2004, vol. 36, pp. 1564–74. https://doi.org/10.1002/sia.1984.
48. T.C. Lin, G. Seshadri, and J.A. Kelber: *Appl. Surf. Sci.*, 1997, vol. 119, pp. 83–92. https://doi.org/10.1016/S0169-4332(97)00167-0.
49. R. Sanchis, D. Alonso-Domínguez, A. Dejoz, M.P. Picom, I. Álvarez-Serrano, T. García, M.L. López, and B. Solsona: *Materials.*, 2018, vol. 11, p. 1387. https://doi.org/10.3390/ma11081387.
50. L. Lu, Z. Ai, J. Li, Z. Zheng, Q. Li, and L. Zhang: *Cryst. Growth Des.*, 2007, vol. 7, pp. 459–64. https://doi.org/10.1021/cg060633a.
51. T. Zhang, Z. Li, L. Wang, Z. Zhang, and S. Wang: *Int. J. Hydrog. Energy.*, 2019, vol. 44, pp. 1610–19. https://doi.org/10.1016/j.ijhydene.2018.11.120.
52. W. Yan, X. Cao, J. Tian, C. Jin, K. Ke, and R. Yang: *Carbon.*, 2016, vol. 99, pp. 195–202. https://doi.org/10.1016/j.carbon.2015.12.011.
53. W. Yan, W. Bian, C. Jin, J.H. Tian, and R. Yang: *Electrochim. Acta.*, 2015, vol. 177, pp. 65–72. https://doi.org/10.1016/j.electacta.2015.02.044.
54. Y. Zhao, G. Nie, X. Ma, P. Xu, and X. Zhao: *Environ. Pollut.*, 2019, vol. 249, pp. 868–77. https://doi.org/10.1016/j.envpol.2019.03.103.
55. M. Fantauzzi, F. Secci, M.S. Angotzi, C. Passiu, C. Cannas, and A. Rossi: *RSC Adv.*, 2019, vol. 9, pp. 19171–79. https://doi.org/10.1039/c9ra03488a.
56. G.B. Ji, S.L. Tang, S.K. Ren, F.M. Zhang, B.X. Gu, and Y.W. Du: *J. Cryst. Growth.*, 2004, vol. 270, pp. 156–61. https://doi.org/10.1016/j.jcrysgro.2004.06.025.
57. K. Tsukimura, S. Sasaki, and N. Kimizuka: *Jpn. J. Appl. Phys.*, 1997, vol. 36, p. 3609. https://doi.org/10.1143/JJAP.36.3609.
58. A.P.G. Rodrigues, D.K.S. Gomes, J.H. Araújo, D.M.A. Melo, N.A.S. Oliveira, and R.M. Braga: *J. Magn. Magn. Mater.*, 2015, vol. 374, pp. 748–54. https://doi.org/10.1016/j.jmmm.2014.09.045.
59. R. Bliem, J. Pavelec, O. Gamba, E. McDermott, Z. Wang, S. Gerhold, M. Wagner, J. Osiecki, K. Schulte, M. Schmid, P. Blaha, U. Diebold, and G.S. Parkinson: *Phys. Rev. B.*, 2015, vol. 92, p. 75440. https://doi.org/10.1103/PhysRevB.92.075440.
60. M. Pardavi-Horvath: *J. Magn. Magn. Mater.*, 2000, vol. 171–183, pp. 215–56. https://doi.org/10.1016/S0304-8853(00)00106-2.
61. P.L. Surman: *Corros. Sci.*, 1973, vol. 13, pp. 113–24. https://doi.org/10.1016/0010-938X(73)90023-1.
62. D.W. Luo and Z.S. Shen: *Acta Metall. Sin.*, 2008, vol. 21, pp. 409–18. https://doi.org/10.1016/S1006-7191(09)60003-X.
63. B. Jeon, Q. Van Overmeere, A.C. Van Duin, and S. Ramanthan: *Phys. Chem. Chem. Phys.*, 2013, vol. 15, pp. 1821–30. https://doi.org/10.1039/C2CP43490C.
64. C. Greyling, A. Kotzi, and P. Viljoen: *Surf. Interface Anal.*, 1990, vol. 16, pp. 293–98. https://doi.org/10.1002/sia.740160161.
65. H. Hong, N.K. Memon, Z. Dong, B.H. Kear, and S. Tse: *Proc. Combust. Inst.*, 2019, vol. 37, pp. 1249–56. https://doi.org/10.1016/j.proci.2018.06.098.
66. F. Genuzio, A. Sala, T. Schmidt, D. Menzel, and H.-J. Freund: *J. Phys. Chem. C.*, 2014, vol. 118, pp. 29068–76. https://doi.org/10.1021/jp504020a.